Intermetallics 174 (2024) 108441

Contents lists available at ScienceDirect

Intermetallics

journal homepage: www.elsevier.com/locate/intermet

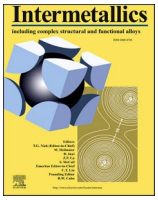

The structural origins of rejuvenation in $Zr_{58}Cu_{22}Fe_8Al_{12}$ bulk metallic glasses

Hao Zhang [a], Longlong Fan [b], Zhong Wang [c], Peter K. Liaw [d], Junwei Qiao [a,e,*]

[a] College of Materials Science and Engineering, Taiyuan University of Technology, Taiyuan, 030024, China
[b] Institute of High Energy Physics, The Chinese Academy of Sciences, Beijing, 100049, China
[c] College of Mechanical and Vehicle Engineering, Taiyuan University of Technology, Taiyuan, 030024, China
[d] Department of Materials Science and Engineering, The University of Tennessee, Knoxville, TN, 37996-2200, USA
[e] Key Laboratory of Interface Science and Engineering in Advanced Materials, Ministry of Education, Taiyuan University of Technology, Taiyuan, 030024, China

ARTICLE INFO

Keywords:
Metallic glasses
Rejuvenation
High-energy synchrotron X-ray diffraction
Nanoindentation
Statistical analysis

ABSTRACT

Combined with the potential energy landscape of metallic glasses, this paper discusses the structural origins of rejuvenation at the atomic, nanoscale, and microscale scales in sequence. At the atomic scale, researchers discovered that the mechanism of rejuvenation undergoes a transformation from 2-atom cluster connections to 3-atom cluster connections, which is beneficial to enhancing ductility. At the nanoscale, it is observed that rejuvenation influences the shear-band nucleation behavior of metallic glasses through statistical analysis of nanoindentation. This process generates a high free volume and a large STZ volume, which make it easier to enhance shear-band density and improve ductility. At the microscale, rejuvenation significantly reduces the nanohardness and elastic modulus of metallic glasses. The increased ductility of rejuvenated metallic glasses can be attributed to the changes in physical quantities at three scales. This study clearly demonstrates the structural origins of rejuvenation in metallic glasses through high-energy synchrotron X-ray diffraction and nanoindentation.

1. Introduction

Bulk metallic glasses (BMGs) have attracted interest due to excellent mechanical and physical properties, such as high strength, large elastic limit, high hardness, and good wear resistance [1,2]. They are expected to be promising structural materials [3]. Due to the absence of work hardening capabilities caused by dislocations and stacking faults as seen in crystalline alloys [4], BMGs fracture abruptly after yielding due to the rapid development of primary shear bands without significant plastic deformation [5,6]. Based on a classic model, the shear transformation zone (STZ) is activated under an external stress, and the shear-band nucleation behavior results from the coalescence of a series of STZs [7,8]. It has been reported that the ductility of BMGs can be enhanced by increasing the free volume through rejuvenation processes such as rapid cooling rates, cryogenic thermal cycling (CTC), and mechanical cycling [9,10]. Facilitating the extensive propagation and entanglement of shear bands are central to these strategies to achieve the strength-ductility synergy [11]. The rejuvenation of heterogeneous structures results in a non-affine thermal strain caused by thermal expansion with a non-affine coefficient in BMGs [12]. Such rejuvenation has been reported to result in higher potential energy and improvements in plasticity and ductility, but a reduction in hardness, and a decrease in compressive strength [13]. Therefore, understanding the structural origins of rejuvenation is crucial for enhancing the plastic deformation capability and designing new BMGs with excellent mechanical properties.

It is well known that the CTC treated BMGs can easily adjust the activation volume to enhance their compression plasticity [11,12]. However, relevant research indicates that the compressive plasticity in BMGs cannot be infinitely improved by simply increasing the number of CTCs [14]. For BMGs with different compositions and various CTC methods, their compression plasticity will result in two distinct changes. Some experimental results with hundreds of the CTC displayed that the compression plasticity will initially increases and then decreases, but there were no fixed breakpoints [15]. Other experimental results with the CTC within one hundred exhibited that the compression plasticity steadily increases as the CTC number increases [16]. The changes in the compression plasticity of BMGs were solely the result of macroscopic

* Corresponding author. College of Materials Science and Engineering, Taiyuan University of Technology, Taiyuan, 030024, China.
E-mail address: qiaojunwei@gmail.com (J. Qiao).

https://doi.org/10.1016/j.intermet.2024.108441
Received 20 May 2024; Received in revised form 20 July 2024; Accepted 29 July 2024
Available online 5 August 2024

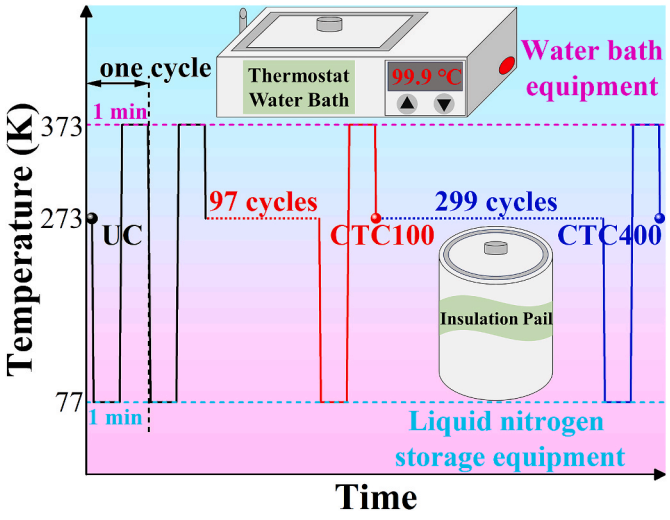

Fig. 1. Schematic diagram of the cryogenic thermal cycling (CTC) is shown. A water bath equipment and a liquid nitrogen storage equipment were used to bring the samples to 373K and 77K, respectively.

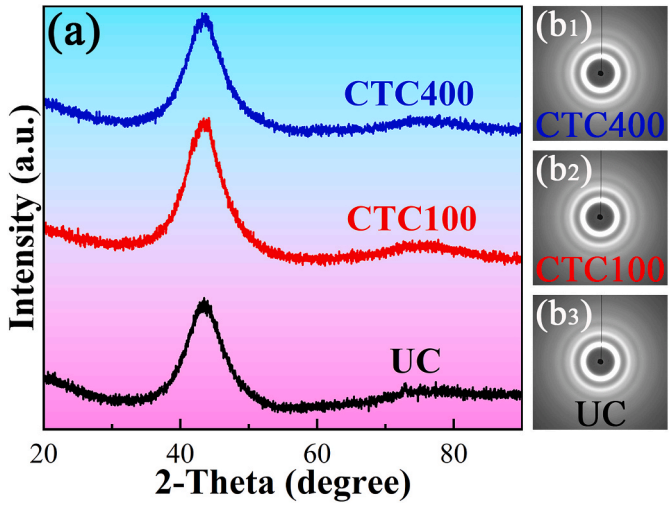

Fig. 2. (a) XRD patterns of UC, CTC100, and CTC400 samples are displayed, respectively. (b) 2D diffraction patterns of three samples are shown respectively.

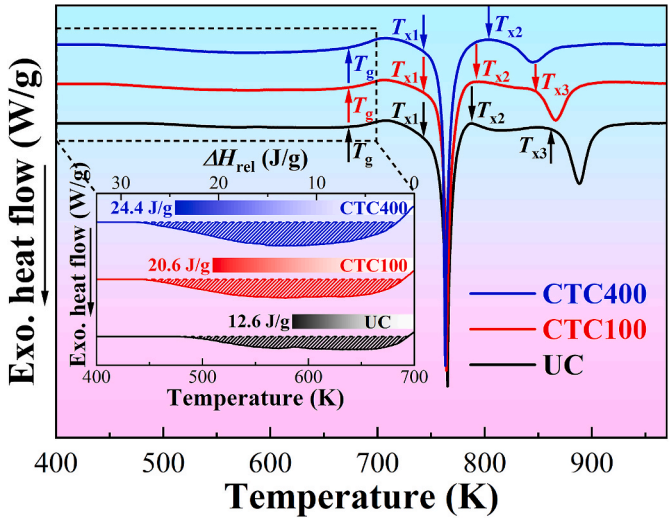

Fig. 3. DSC curves of UC, CTC100, and CTC400 samples are shown, respectively. The relaxation enthalpies of the three samples are shown in the inset, respectively.

mechanical behavior influenced by rejuvenation. In the current study, the structural origin of rejuvenation in BMGs is investigated by subjecting a Zr-based BMG to three different states using the CTC, namely UC, CTC100, and CTC400. High-energy synchrotron X-ray diffraction has been proven to be a very useful tool for studying the atomic-scale structures of BMGs [17,18]. Liu et al. [19] revealed that medium-range order endows Zr-based bulk metallic glass with excellent tensile plasticity through in-situ high-energy synchrotron X-ray diffraction. Nanoindentation has been verified as an effective tool for investigating the microscopic mechanical behavior [20,21]. In authors' previous study, the activation volume and the number of atoms based on a new Berkovich increased as the number of CTCs increases in $Zr_{58}Cu_{22}Fe_8Al_{12}$ bulk metallic glass [22]. Based on high-energy synchrotron X-ray diffraction, the atomic-scale structural evolution of three samples is revealed by analyzing static-structure factors and pair-distribution functions. The structural evolution at the nanoscale and microscale, as well as the shear-band nucleation behavior of three samples, are determined through the statistical analysis of nanoindentation. Based on the potential energy landscape, the structural origins of rejuvenation in BMGs are analyzed sequentially across three scales.

2. Experimental details

2.1. Preparation of the samples

The Zr-based BMG ($Zr_{58}Cu_{22}Fe_8Al_{12}$, at.%) ingots were produced by arc melting mixtures of high-purity (above 99.9 %, weight percent) constituent metals under a high-purity argon atmosphere, achieved by melting pure titanium. The ingots were remelted five times to ensure chemical homogeneity and then sucked into a water-cooled copper crucible to produce alloy plates with a thickness of 2 mm. The experiment-sized square plates, with the dimensions of 2 mm (thickness) × 5 mm (width) × 5 mm (length), were cut from alloy plates. These plates were thinned to 1 mm using coarse sandpapers, and then all double-grinded and polished to achieve identical thickness (~0.9 mm). The thickness of the square plates was reduced to 1 mm using coarse sandpapers. Subsequently, both surfaces of the square plates were ground and polished to achieve ideal states. During the rejuvenation treatment, one complete cycle was first immersed in liquid nitrogen for 1 min and then dipped into a constant-temperature water bath at 373 K for 1 min, as shown in Fig. 1. The square plates were named UC (unchanged), CTC100 and CTC400 after 0, 100 and 400 complete cycles, respectively. Three samples were scanned from 20° to 90° at a scanning speed of 5°/minute using X-ray diffraction with Co-*K*α radiation to examine their fully glass structures, as shown in Fig. 2(a).

2.2. Characterization

2.2.1. High-energy synchrotron X-ray diffraction measurements

High-energy synchrotron X-ray diffraction measurements were performed on UC, CTC100, and CTC400 samples at the 3W1 beamline, Beijing Synchrotron Radiation Facility (BSRF). A high-energy X-ray with a beam size of 700 μm × 700 μm and a wavelength of 0.2099 Å was used for data collection. Two-dimensional (2D) diffraction patterns were obtained using an iRay Mercu1717HS image plate detector, as displayed in Fig. 2(b). The static structure factor, $S(Q)$, was derived from the two-dimensional diffraction ring patterns by masking bad pixels, integrating images, subtracting the appropriate background, and correcting for oblique incidence, absorption, multiple scattering, Compton scattering, and Laue correction using Fit2D and PDFgetX2 [23]. The reduced pair distribution function (PDF), $G(r)$, was obtained by Fourier transforming

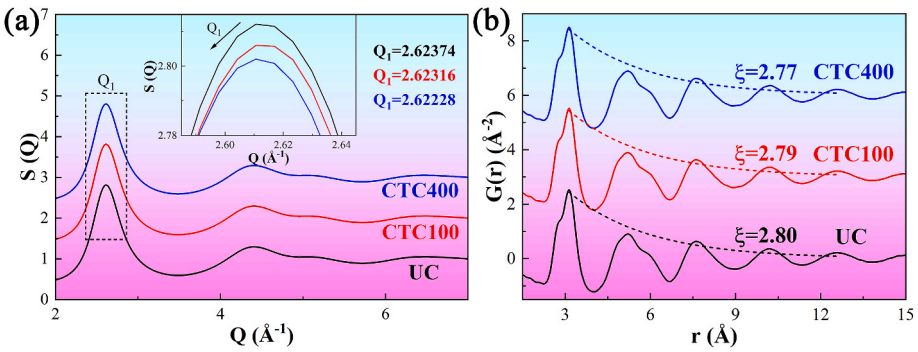

Fig. 4. (a) The static-structure factor, $S(Q)$, was determined for UC, CTC100, and CTC 400 samples of the Zr-based metallic glass. The inset shows the variation in the position of the first sharp diffraction peak position, Q_1, for three samples. (b) The exponential functions are used to fit the reduced pair distribution function (PDF), $G(r)$, for three samples.

$S(Q)$,

$$G(r) = \frac{2}{\pi}\int_0^{Q_{max}} Q[S(Q)-1]\sin(Qr)\mathrm{d}Q = 4\pi r[\rho(r)-\rho_0] \quad (1)$$

where r is the real space distance, ρ_0 is the average number density, and $\rho(r)$ is the microscopic number density [24].

2.2.2. Differential scanning calorimetry measurements

Differential scanning calorimetry (DSC) measurements were purposed to obtain the thermal parameters. Three samples were heated from room temperature (303 K) to 973 K at a constant heating rate of 20 K/min under a flowing high-purity argon atmosphere. As shown in Fig. 3, the CTC would not affect the glass transition temperature and the starting temperature of the first crystallization, but it would lower the starting temperature of the third crystallization. Even the second and third crystallizations of the CTC400 sample combined together. The

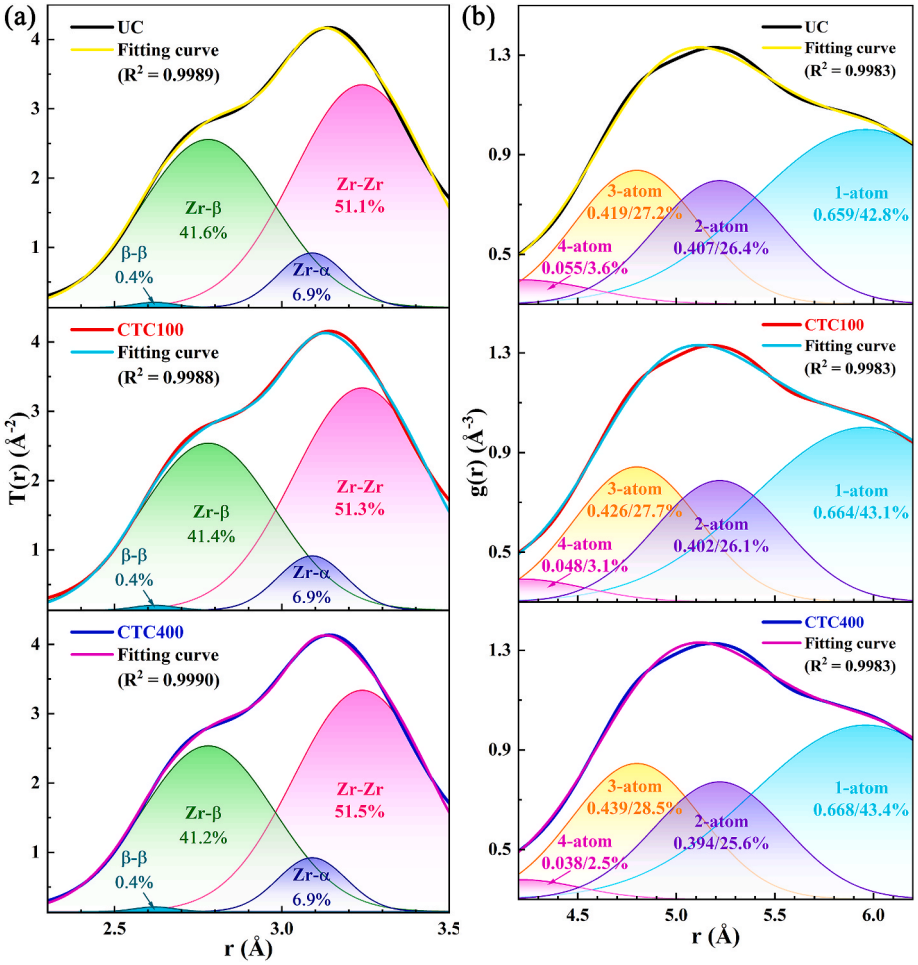

Fig. 5. (a) Gaussian functions are used to form the best fit of the first-shell peaks of PDFs, $T(r)$, for three samples. Four major partials are decomposed for three samples, respectively. (b) Gaussian functions are used to form the best fit for the second coordination shell in pair-distribution functions, $g(r)$. And four atom-cluster connections for three samples were respectively corresponded to the decomposed partials.

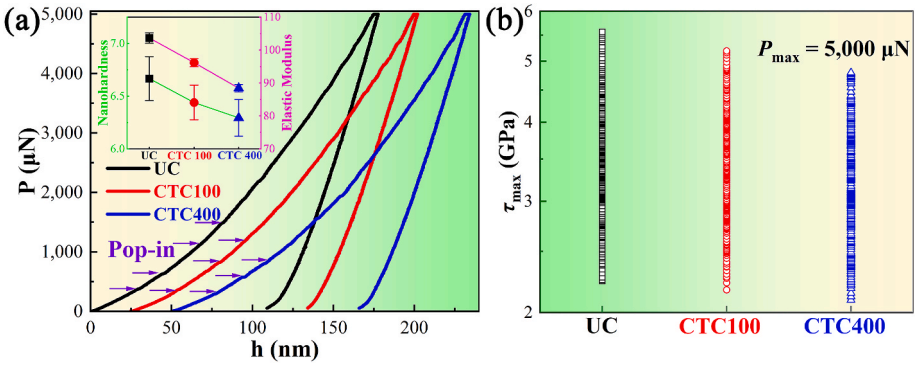

Fig. 6. (a) The *P-h* curves of UC, CTC100, and CTC400 samples, respectively. The inset describes the variation in nano-hardness and elastic modulus of three samples. (b) The distribution of τ_{max} among UC, CTC100, and CTC400 samples, respectively.

relaxation enthalpy of the three samples was calculated via integrating the DSC curves, as displayed in the inset of Fig. 3 [25]. It can be seen intuitively that with the number of CTCs increases, the relaxation enthalpies of three samples are 12.6 J/g, 20.6 J/g and 24.4 J/g, respectively. Thus, the degree of rejuvenation of the Zr-based bulk metallic glass increases as the number of CTCs increases.

2.2.3. Nanoindentation measurements

A relatively blunt Berkovich diamond indenter was used to conduct nanoindentation (Bruker, Minneapolis, MN, USA) measurements at room temperature. The displacement resolution of the machine was less than 0.01 nm, and the load resolution were less than 50 nN. In order to ensure thermal stability, the standard fused silicon was used to calibrate the instrument at least 30 min before measurements, until the thermal drift was below 0.05 nm/s. Nanoindentation tests were conducted in a load-control mode with a maximum load of 5 mN, a loading rate of 1 mN/s, an unloading rate of 1 mN/s, and a fixed holding time of 2 s. To ensure a statistically significant dataset from the applied load (P) and penetration depth (h) curve, precisely 200 tests were carried out on UC, CTC100, and CTC400 samples.

3. Results

3.1. Influence of rejuvenation in high-energy synchrotron X-ray diffraction

Fig. 4(a) shows the static-structure factors of UC, CTC100, and CTC400 samples. All samples exhibit a prominent initial peak, and the oscillations to the right of the peak decrease rapidly. The first diffraction peak, Q_1, gradually shifts to the left with an increase of rejuvenation, as exhibited in the inset of Fig. 4(a). The peak position of Q_1 is positively correlated with the sample density [26]. The densities of three samples decrease successively as rejuvenation increases, indicating that rejuvenation can induce a more loosely packed structure. According to the peak position, Q_1, the atomic volume, V_a, can be calculated by $Q_1 \bullet V_a^{0.433} = 9.36$ [27]. The atomic volumes of UC, CTC100, and CTC400 samples were determined to be 18.8646 Å^3, 18.8742 Å^3, and 18.8888 Å^3, respectively. According to the relationship between the atomic volume and the free volume, V_f, the free volume can be obtained by $V_f = V_a - V_0$, and $V_a = V_f/(1-n)$, where V_0 is the average atomic volume [28]. The basic percentage of free volumes in the average atomic volume was taken as 5 % through XRD and DSC measurements, indicating that the importance of n is 95 % [29]. The free volumes of UC, CTC100, and CTC400 samples were calculated to be 0.9432 Å^3, 0.9437 Å^3, and 0.9444 Å^3, respectively. It can be clearly stated that as rejuvenation increases, the density decreases, while both the atomic volume and the free volume increase.

The mechanical properties of metallic glasses can be affected by the atomic-scale topological order [30]. As exhibited in Fig. 4(b), the reduced pair-distribution functions (PDF), G(r), provide the structural information about the UC, CTC100, and CTC400 samples in real space. Applying an exponential decay function is an effective method to estimate the decrease in the peak height of the PDF. The function is $f(r) = A \bullet \exp(-r/\xi)$, here the parameter ξ is used to measure the ordering degree [31]. A more disordered structure results in a smaller ξ value. The ξ values of UC, CTC100, and CTC400 samples were fitted to be 2.80, 2.79, and 2.77, respectively. Therefore, as rejuvenation increases, the sample exhibits a more disordered structure, which is beneficial to ductility and toughness of metallic glasses. This is achieved by accumulating more space to dissipate energy.

To better resolve the nearest neighbor part of the first PDF peaks, $T(r)$ is converted from $G(r)$ through the equation, $T(r) = 4\pi\rho_0 r + G(r)$ [32]. As displayed in Fig. 5(a), the atomic pair distribution of UC, CTC100, and CTC400 samples conforms to a Gaussian distribution. In the fitting process, four major partials should be considered, such as Zr–Zr, Zr-α (Zr–Al), and two "compounded" partials: Zr-β (consisting of two sub-partials: Zr–Cu, Zr–Fe) and β-β (consisting of two sub-partials: Cu–Cu, Cu–Fe, Fe–Fe). The initial weight factors of the Zr-based BMG are 0.501 (Zr–Zr), 0.067 (Zr-β), 0.365 (Zr-α), and 0.067 (β-β), respectively, which are calculated by the methods in Ref. [33]. The best-fit peak positions are 3.24 Å (Zr–Zr), 3.09 Å (Zr-β), 2.78 Å (Zr-α), and 2.62 Å (β-β), respectively, which are derived from the values in Ref. [34]. Compared to the fitting ratios of three samples in the text of Fig. 5(a), it can be clearly concluded that the fitting ratio of the Zr–Zr bond increases as rejuvenation increases. A larger ratio indicates a looser atomic packing of the nearest neighbors. Based on the related conclusion regarding the peak position, the free volume of real space increases with rejuvenation in the nearest coordination shell [35].

It is worth noted that the splitting of the second PDF peak for each sample describes the atomic packing around the next nearest neighbors [26]. The pair distribution function, $g(r)$, is transformed from $G(r)$ via the equation, $g(r) = 1 + G(r)/(4\pi\rho_0 r)$. At the medium-range order (MRO) length scale, the connection between the short-range order (SRO) clusters is highly related to the second peak of $g(r)$ [36]. Here, SRO clusters have four connection modes: intercross-shared, face--shared, edge-shared, and vertex-shared, which are referred to as 4-atom, 3-atom, 2-atom, and 1-atom modes [37]. It is well known that these connection modes may have been affected during the deformation process [38]. Based on the coordinating atomic-weighted bond length, the average atomic radius, R, of SRO can be calculated to be 2.98 Å. The distance between the two centers of the SRO-clusters can be calculated as 4.21 Å ($\sqrt{2}R$), 4.80 Å ($\sqrt{8/3}R$), 5.22 Å ($\sqrt{3}R$), and 5.96 Å ($2R$) for the four connection modes, respectively [39]. As exhibited in Fig. 5(b), the Gaussian fitting with four different connection methods was applied to the second peak. The initial values of the theoretical distances, as well as

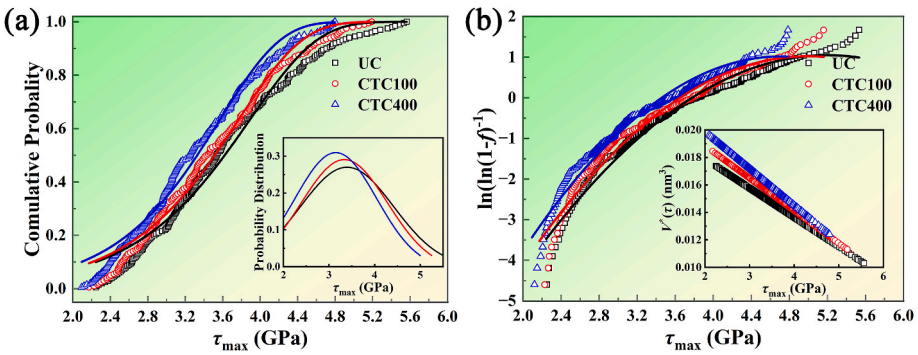

Fig. 7. (a) The fitting degrees of the cumulative probability distributions of τ_{max} all are 0.98 for UC, CTC100, and CTC400 samples. The probability distributions of τ_{max} are exhibited in the inset for three samples. (b) The fitting degrees between $ln\left[ln\,(1-f)^{-1}\right]$ and τ_{max} all are 0.96 for UC, CTC100, and CTC400 samples. The range of V^* are exhibited in the inset for three samples.

the specific areas and proportions of the four connection modes, are listed in the text of Fig. 5(b). With the increase of rejuvenation, the 1-atom and 3-atom MROs increase, while the 2-atom and 4-atom MROs decrease. This suggests that the non-thermal effect of rejuvenation loosens the structure of metallic glasses by weakening the MROs. Meanwhile, the variation of MROs results in a lower packing density with increasing rejuvenation, which is consistent with the above findings. Liu et al. suggested that the plasticity can be controlled by varying the 2-atom and 3-atom connection modes [19]. Therefore, the change of connection modes regulated by rejuvenation is more favorable for the ductility during the deformation process.

3.2. The influence of rejuvenation in nanoindentation

Fig. 6(a) exhibits the representative nanoindentation (*P-h*) curves of UC, CTC100, and CTC400 samples. In order to facilitate subsequent observation and analysis, the curves of the latter two samples are shifted by 25 nm and 50 nm along the displacement axis, respectively. With the softening effect caused by increasing cycles, the first pop-in appears later, as indicated by the purple arrow in Fig. 6(a). The variation in the formation and propagation of the shear bands during the indentation process in BMGs can be attributed to this phenomenon [40]. Due to the increase of the flow-defect concentration associated with the amount of free volumes [41], the nano-hardness values of three samples were 6.67 ± 0.21, 6.44 ± 0.16, and 6.29 ± 0.17 GPa, respectively, as displayed in the inset of Fig. 6(a). In addition, the elastic moduli of three samples were 103.6 ± 1.6, 96.1 ± 1.2, and 88.4 ± 1.1 MPa, respectively. Rejuvenation causes relaxation of the internal structure and material softening, resulting in a decrease in the nano-hardness and elastic modulus. It is well known that STZs are the basic units that can withstand the plastic deformation, rather than structural defects, and their size can reflect the degree of plasticity in BMG [42,43]. STZs are calculated through statistical analysis of the shear-stress data generated from pop-ins (marking the elastoplastic transition).

It is necessary to extract the effective serrations from the *P-h* curves before conducting the statistical analysis of the shear stress. In order to ensure the correctness of the statistical analysis, large amounts of noise serrations should be eliminated through the noise-reduction methods. The comprehensive operational details have been published in Ref. [22]. The effective serrations were defined as the strain bursts on the *P-h* curves and were viewed as a yield point of the macroscopic stress-strain curves. During each loading of the spherical indenter, the initial pop-ins can be regarded as the effective serrations, marking the transition from the instantaneous elastic strain to plastic deformation [44]. During each loading of the Berkovich diamond indenter, the first pop-in event is identified to calculate the maximum shear stress, $\tau_{\max}$ [45]. Thus, $\tau_{\max}$ can be calculated by using the following equation,

$$\tau_{\max} = \frac{P}{24.56 \times 3 \times \sqrt{3} \cdot (h - \varepsilon P/S)^2}. \tag{2}$$

where $\varepsilon = 0.75$ is a constant, and S is the contact stiffness. It can be clearly seen that τ_{max} shows the overall decline as the number of CTC increases, as displayed in Fig. 6(b). The variation of τ_{max} was attributed to the effect of the CTC, which sequentially increases the free volume of three samples [14,16].

The statistics of $\tau_{\max}$ were analyzed in three samples, and their cumulative probability distributions were illustrated in Fig. 7(a). Therefore, the cumulative distribution function, f, is

$$f = 1 - \exp\left[- \exp\left(\frac{V^*}{kT}\tau_{\max} + A\right)\right], \tag{3}$$

where k is the Boltzmann constant, T is the absolute temperature, $A = \Delta F^*/kT + \ln[kT/V^*(d\tau/dT)]$ can be considered as a constant, and the activation volume, V^*, can be obtained as follows,

$$\ln\left[\ln\,(1-f)^{-1}\right] = A + \left(\frac{V^*}{kT}\right)\tau_{\max}. \tag{4}$$

However, there are non-linear slopes in three curves, as shown in Fig. 7(b). It can be addressed by combining a first-order polynomial [45].

$$V^*(\tau) = V_0 + V_1\tau_{\max}, \tag{5}$$

where V_0 and V_1 are fitting parameters.

According to the cooperative shear model (CSM) proposed by Johnson and Samwer [46], the STZ volume, Ω, of three samples was calculated using the determined V^*.

$$\Omega = \frac{\tau_0}{6R_0G\gamma_C^2\zeta(1-\tau/\tau_0)^{1/2}}V^*, \tag{6}$$

where $G = 32.5$ GPa is the shear modulus [44], $\gamma_C = \tau/G$ is the critical shear strain, τ is numerically equal to $\tau_{\max}$, and τ_0 is the threshold shear strength at 0 K. R_0, ζ, and γ_C are constants, and respectively approximately equal to 1/4, 3, and 0.027. Combined with $\tau_0/G = 0.036$, τ/τ_0 can be obtained as follows,

$$\gamma_C = \tau \Big/ G = \gamma_{C0} - \gamma_{C1}\left(T/T_g\right)^{2/3}, \tag{7}$$

where $\gamma_{C0} = 0.036 \pm 0.002$, $\gamma_{C1} = 0.016 \pm 0.002$, and $T_g = 677$ K is the glass transition temperature [47]. Based on the dense-packing hard-sphere model in BMGs, the average atomic radius is $R = \left(\sum_i^n A_i r_i^3\right)^{\frac{1}{3}}$, wherein A_i is the atomic fraction of each element and r_i is the atomic

Table 1
The activation volume, V^*, the STZ volume, Ω, and the number of atoms in an STZ, N for three CTC samples.

	V^* (nm^3)	Ω (nm^3)	N (atom)
UC	0.0138 ± 0.0035	0.305 ± 0.078	22 ± 6
CTC100	0.0149 ± 0.0036	0.328 ± 0.079	24 ± 6
CTC400	0.0160 ± 0.0036	0.353 ± 0.080	26 ± 6

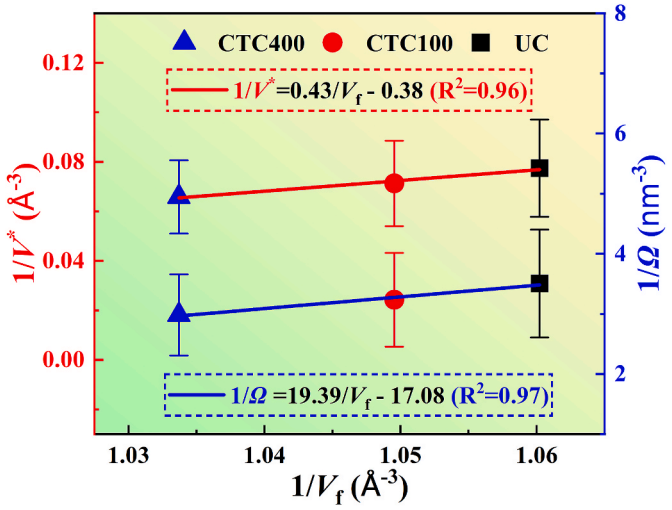

Fig. 8. The red line describes a linear relationship between the reciprocal of the activation volume, $1/\Delta V^*$, and the reciprocal of the free volume, $1/V_f$. The blue line describes a linear relationship between the reciprocal of the activation volume, $1/\Omega$, and the reciprocal of the free volume, $1/V_f$.

radius of each element [48]. The number of atoms in an STZ, N, can be estimated by the calculated Ω. The number of atoms in an STZ, the STZ volume, and the activation volume of three samples were listed in Table 1. It can be intuitively observed that three parameters gradually increase with rejuvenation. More free volumes are introduced into metallic glasses through rejuvenation, leading to a decrease in interatomic bonding strength, an increase in atomic spacing, and a larger volume and size of STZ [49,50].

4. Discussion

4.1. The relationship between the free volume, activation volume and STZ volume

The free volume theory was rigorously established based on the forward jump of single atoms under the action of sufficient free volume and shear force [51]. The free volume theory has been used to study the stress drop and the strain rise behavior on the stress-strain curve of BMGs [52,53]. The CSM was carefully established was established based on the formation of activated STZs by dozens of atoms due to the action of shear force [46]. The CSM has been used to study the temperature-dependent shear behavior mechanism in BMGs [54,55]. The connection between the free volume and the activation volume of the two theories could be considered to be bidirectional, and the relevant activation factor from the free volume theory can be incorporated into the CSM [56]. Hence, the relationship was articulated as

$$C\dot{\gamma} = \omega_0 \exp\left(-\frac{W_\tau}{kT}\right)\exp\left(-\frac{\Delta V^*}{V_f}\right), \tag{8}$$

where C is a dimensionless constant, $\dot{\gamma}$ is the strain rate, ω_0 is an attempt frequency, and the barrier energy for the STZ,

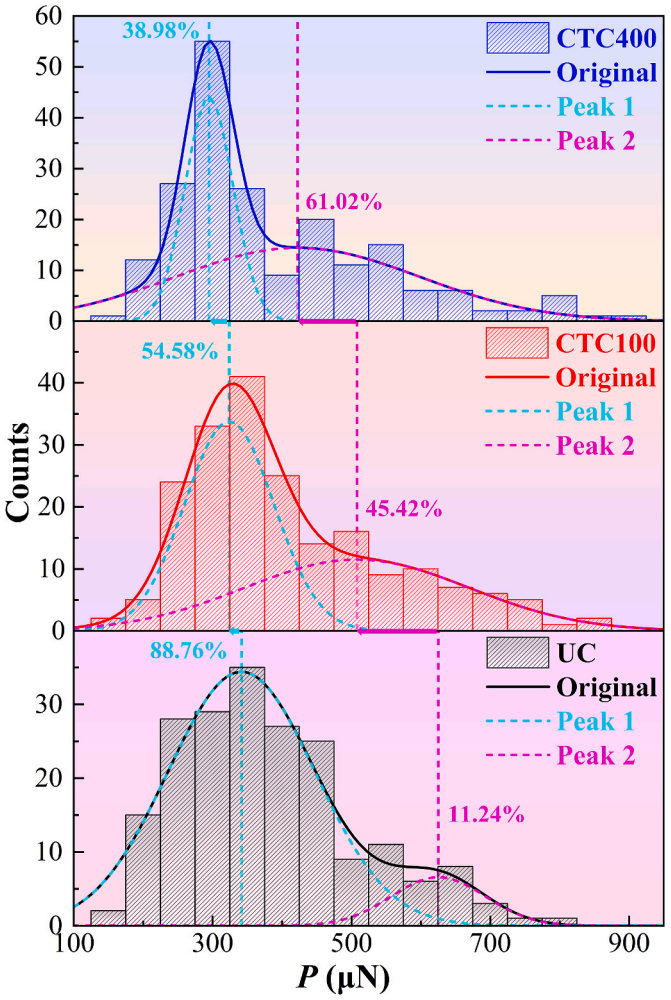

Fig. 9. Histograms and fitting results by Gaussian distributions for UC, CTC100, and CTC 400 samples. The fraction of each peak is given, and the dashed line marks the average P value of each peak.

$$W_\tau = 4RG\gamma_C^2\left(1-\frac{\tau}{\tau_0}\right)^{3/2}\zeta\Omega. \tag{9}$$

Combined with Eq. (6), the relationship between W_τ and ΔV^* is

$$W_\tau = 2/3(\tau_0-)\tau)\Delta V^*. \tag{10}$$

Taking the logarithm of both sides of Eq. (8), and simplifying it as

$$\frac{\ln(\omega_0/C\dot{\gamma}) - W_\tau/kT}{\Delta V^*} = \frac{1}{V_f}. \tag{11}$$

Submitted Eq. (10) into Eq. (11), and the relationship between V_f and ΔV^* can be found that

$$\frac{1}{\Delta V^*} = k_1\frac{1}{V_f} + b_1, \tag{12}$$

where $k_1 = 1/\ln(\omega_0/C\dot{\gamma})$, and $b_1 = 2(\tau_0-\tau)/[3kT\ln(\omega_0/C\dot{\gamma})]$. It can be intuitively obtained that the reciprocal of the activation volume, $1/\Delta V^*$, has a linear relationship with the reciprocal of the free volume, $1/V_f$, as the CTC increases by substituting the experimental data into Eq. (12). As exhibited by the red line in Fig. 8, there is a linear relationship, $1/\Delta V^* = 0.43/V_f - 0.38$, and the degree of fitting is $R^2 = 0.96$.

It is easily understood that the increase in free volume will accompany with an increase in activation volume as the CTC increases, which will further affect the shear mechanism. As mentioned before, the direct

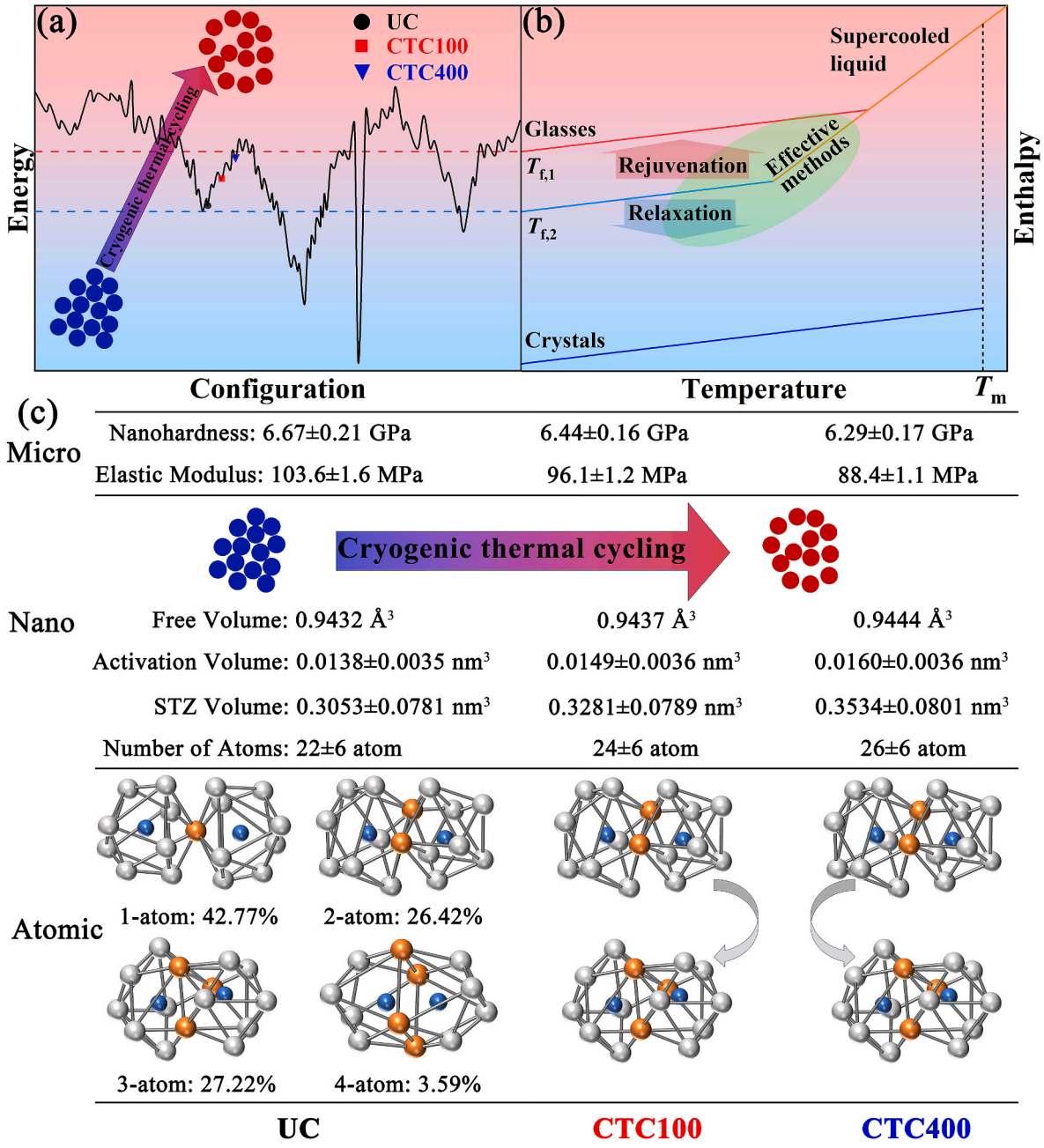

Fig. 10. (a) The potential energy landscape for various possible states in metallic glasses. (b) Thermodynamic pictures of metallic glasses with various T_f, and the effect of rejuvenation and relaxation on the thermodynamic states by effective methods. (c) The differences among UC, CTC100, and CTC 400 samples at an atomic scale, a nanoscale and a microscale.

impact is the reduction of the nano-hardness and elastic modulus with the increase of CTC. Similarly, by submitting Eq. (9) into Eq. (11), the relationship between V_f and Ω can be derived that

$$\frac{1}{\Omega} = k_2 \frac{1}{V_f} + b_2, \tag{13}$$

where $k_2 = 6R_0G\gamma_C^2\zeta(1-\tau/\tau_0)^{1/2}/[\tau_0 \ln(\omega_0/C\dot{\gamma})]$, and $b_2 = 4RG\gamma_C^2\zeta(1-\tau/\tau_0)^{3/2}/kT \ln(\omega_0/C\dot{\gamma})$. The activation volume and the STZ volume have a linear relationship as shown in Eq. (6). With the CTC increases, it can also be observed that the reciprocal of the STZ volume, $1/\Omega$, has a linear relationship with the reciprocal of the free volume, $1/V_f$, by substituting the experimental data into Eq. (13). As displayed by the blue line in Fig. 8, the line relationship is $1/\Omega = 19.39/V_f - 17.08$, the fitting degree is $R^2 = 0.97$.

4.2. The effect of rejuvenation in shear-band nucleation behavior

Fig. 9 shows the statistical analysis of the load at the maximum shear stress for UC, CTC100, and CTC400 samples, illustrating the impact of rejuvenation on the shear-band nucleation behavior. Perepezko *et al.* [57] asserted the presence of two intrinsic defect sites that triggered the formation of initial shear bands. This conclusion was drawn from the datasets obtained on four different metallic glasses, which exhibited a bimodal distribution. Thus, two Gaussian functions are used to fit the count plots of three samples effectively. Therefore, there are two shear-band nucleation sites for the Zr-based BMG: a high-load nucleation site and a low-load nucleation site. After rejuvenation, the two

nucleation sites of the shear bands move to a lower load overall, indicating a significant increase of free volume content in metallic glasses [12]. A high free-volume content weakens the activation load of the STZ, which is favorable for the shear-band mediated ductility [11]. Therefore, the load required for the shear-band nucleation gradually decreases due to the influence of rejuvenation [58]. Furthermore, due to the influence of CTC, the proportion of the low-load nucleation site steadily decreases, whereas the proportion of the high-load nucleation site steadily increases. The shift is one of the reasons for the formation of larger STZs during the shear-band nucleation process. Larger STZs can induce fewer STZs to activate the shear-band nucleation than smaller STZs [59]. STZs with larger volumes lead to easily generate and multiply shear bands, which can increase the shear-band density, plastic zone, and ductility in BMGs [60].

4.3. The structural origins of rejuvenation

The potential energy landscape (PEL) illustrates the different potential states in metallic glasses, as depicted in Fig. 10(a). It can be clearly seen that there is more free-volume content in the loosely packed regions due to the atomic motion. This is because that BMGs form a denser atomic packing after rejuvenation, which increases the elastic fluctuations by broadening the energy-barrier distribution [14]. Therefore, the Zr-based BMG transitions from a densely packed structure to a loosely packed structure, from a low energy state to a high energy state, and from a low T_f value to a large T_f value [58]. As exhibited in Fig. 10 (b), rejuvenation leads to higher T_f states, resulting in looser packed structures and increasing ductility [16]. On the contrary, relaxation results in lower T_f states, which lead to denser packed structures and more brittle metallic glasses [61]. Fig. 10(c) illustrates the variances at an atomic scale, a nanoscale, and a microscale among three samples. From the atomic scale, the fractions of 1-atom and 3-atom cluster connections increase, whereas the fractions of 2-atom and 4-atom cluster connections decrease. Among them, the transition from 2-atom cluster connections to 3-atom cluster connections is considered to be more beneficial for ductility [19]. At the nanoscale, the number of atoms in an STZ, STZ volume, activation volume, and free volume all steadily increase due to changes in atomic cluster connections. Both the high free volumes and large STZs are beneficial for the ductility of metallic glasses [62]. From the microscale, the nano-hardness and elastic modulus are significantly reduced due to the increase in high free volumes and activation volumes in metallic glasses [45]. The change in behavior at the three scales results in denser shear bands with high free volumes and STZ volumes due to stress concentrations, leading to improve ductility of metallic glasses at the macroscopic scale.

5. Conclusions

In summary, the paper combines high-energy synchrotron X-ray diffraction and nanoindentation to investigate the structural origins of rejuvenation in metallic glasses. Firstly, the analysis of high-energy synchrotron X-ray diffraction reveals an increase of free volumes in metallic glasses. The analysis of high-energy synchrotron X-ray diffraction also exhibits that rejuvenation affects the connections between four distinct atomic clusters, causing them to undergo transformation into one another. Especially, converting 2-atom cluster connections to 3-atom cluster connections can effectively enhance ductility. Secondly, the statistical analysis of nanoindentation indicates that rejuvenation effectively increases the number of atoms in an STZ, STZ volume, and activation volume by influencing the shear-band nucleation behavior. Finally, combined with the potential energy landscape of metallic glasses, the structural origins of rejuvenation are discussed from the atomic scale, the nanoscale, and the microscale. The increased ductility of rejuvenation in metallic glasses can be attributed to the physical properties change at three different scales.

CRediT authorship contribution statement

Hao Zhang: Writing – original draft, Visualization, Validation, Supervision, Software, Resources, Methodology, Investigation, Formal analysis, Data curation, Conceptualization. **Longlong Fan:** Software, Formal analysis. **Zhong Wang:** Project administration, Funding acquisition. **Peter K. Liaw:** Writing – review & editing, Validation, Funding acquisition. **Junwei Qiao:** Writing – review & editing, Visualization, Validation, Supervision, Funding acquisition, Formal analysis.

Declaration of competing interest

The authors declare that they have no known competing financial interests or personal relationships that could have appeared to influence the work reported in this paper.

Data availability

Data will be made available on request.

Acknowledgement

J.W.Q. would like to acknowledge the financial support of the National Natural Science Foundation of China (No. 52071229). Z.W. would like to acknowledge the financial support of the National Natural Science Foundation of China (No. 52201188), and the Research Project of Shanxi Council of China (No. 2022-037). P.K.L. very much appreciates the support from the National Science Foundation (DMR - 1611180, 1809640, and 2226508). The X-ray pair distribution function measurements were performed at the 3W1 beamline, Beijing Synchrotron Radiation Facility (BSRF).

References

[1] M.M. Trexler, N.N. Thadhani, Mechanical properties of bulk metallic glasses, Prog. Mater. Sci. 55 (8) (2010) 759–839.
[2] W.H. Wang, The elastic properties, elastic models and elastic perspectives of metallic glasses, Prog. Mater. Sci. 57 (3) (2012) 487–656.
[3] Y.Q. Cheng, E. Ma, Atomic-level structure and structure–property relationship in metallic glasses, Prog. Mater. Sci. 56 (4) (2011) 379–473.
[4] Z. Zhang, C. Wang, P. Liu, K.M. Reddy, X. Wang, M. Chen, S. Song, Deformation behavior of a nanoporous metallic glass at room temperature, Int. J. Plast. 152 (2022).
[5] A.L. Greer, Y.Q. Cheng, E. Ma, Shear bands in metallic glasses, Mater. Sci. Eng. R Rep. 74 (4) (2013) 71–132.
[6] C. Schuh, T. Hufnagel, U. Ramamurty, Mechanical behavior of amorphous alloys, Acta Mater. 55 (12) (2007) 4067–4109.
[7] M.L. Falk, J.S. Langer, L. Pechenik, Thermal effects in the shear-transformation-zone theory of amorphous plasticity: comparisons to metallic glass data, Phys. Rev. 70 (1) (2004) 011507.
[8] B. Kondori, A. Amine Benzerga, A. Needleman, Discrete shear-transformation-zone plasticity modeling of notched bars, J. Mech. Phys. Solid. 111 (2018) 18–42.
[9] J.E.K. Schawe, J.F. Löffler, Existence of multiple critical cooling rates which generate different types of monolithic metallic glass, Nat. Commun. 10 (1) (2019) 1337.
[10] L.T. Zhang, Y.J. Wang, E. Pineda, Y. Yang, J.C. Qiao, Achieving structural rejuvenation in metallic glass by modulating β relaxation intensity via easy-to-operate mechanical cycling, Int. J. Plast. 157 (2022).
[11] Y. Tang, H. Zhou, H. Lu, X. Wang, Q. Cao, D. Zhang, W. Yang, J.Z. Jiang, Extra plasticity governed by shear band deflection in gradient metallic glasses, Nat. Commun. 13 (1) (2022) 2120.
[12] S.V. Ketov, Y.H. Sun, S. Nachum, Z. Lu, A. Checchi, A.R. Beraldin, H.Y. Bai, W. H. Wang, D.V. Louzguine-Luzgin, M.A. Carpenter, A.L. Greer, Rejuvenation of metallic glasses by non-affine thermal strain, Nature 524 (7564) (2015) 200–203.
[13] T.J. Lei, L.R. DaCosta, M. Liu, W.H. Wang, Y.H. Sun, A.L. Greer, M. Atzmon, Microscopic characterization of structural relaxation and cryogenic rejuvenation in metallic glasses, Acta Mater. 164 (2019) 165–170.
[14] Y. Zhu, Y. Zhou, A. Wang, H. Li, H. Fu, H. Zhang, H. Zhang, Z. Zhu, Atomic-scale icosahedral short-range ordering in a rejuvenated Zr-based bulk metallic glass upon deep cryogenic treatment, Mater. Sci. Eng., A 850 (2022) 143565.
[15] L. Wang, Z. Wang, W. Chu, X. Zhao, L. Hu, Evolution path of metallic glasses under extensive cryogenic thermal cycling: rejuvenation or relaxation? Mater. Sci. Eng., A 850 (2022).
[16] S. Zhang, B. Shi, J. Wang, Y. Xu, P. Jin, Rejuvenation of a naturally aged bulk metallic glass by elastostatic loading, Mater. Sci. Eng., A 806 (2021) 140843.

[17] Y.H. Meng, S.Y. Zhang, W.H. Zhou, J.H. Yao, S.N. Liu, S. Lan, Y. Li, Rejuvenation by enthalpy relaxation in metallic glasses, Acta Mater. 241 (2022) 118376.

[18] S. Lan, Y. Ren, X.Y. Wei, B. Wang, E.P. Gilbert, T. Shibayama, S. Watanabe, M. Ohnuma, X.L. Wang, Hidden amorphous phase and reentrant supercooled liquid in Pd-Ni-P metallic glasses, Nat. Commun. 8 (2017) 14679.

[19] S. Liu, W. Dong, Z. Ren, J. Ge, S. Fu, Z. Wu, J. Wu, Y. Lou, W. Zhang, H. Chen, W. Yin, Y. Ren, J. Neuefeind, Z. You, Y. Liu, X.-L. Wang, S. Lan, Medium-range order endows a bulk metallic glass with enhanced tensile ductility, J. Mater. Sci. Technol. 159 (2023) 10–20.

[20] I.-C. Choi, Y. Zhao, B.-G. Yoo, Y.-J. Kim, J.-Y. Suh, U. Ramamurty, J.-i. Jang, Estimation of the shear transformation zone size in a bulk metallic glass through statistical analysis of the first pop-in stresses during spherical nanoindentation, Scripta Mater. 66 (11) (2012) 923–926.

[21] W.H. Zhou, F.H. Duan, Y.H. Meng, C.C. Zheng, H.M. Chen, A.G. Huang, Y.X. Wang, Y. Li, Effect of alloying oxygen on the microstructure and mechanical properties of Zr-based bulk metallic glass, Acta Mater. 220 (2021) 117345.

[22] H. Zhang, Z. Wang, P.K. Liaw, J.W. Qiao, A criterion of the critical threshold of the maximum shear stress in bulk metallic glasses with cryogenic thermal cycling by statistics in nanoindentation, Mater. Sci. Eng., A 873 (2023) 145031.

[23] X. Qiu, J.W. Thompson, S.J.L. Billinge, PDFgetX2: a GUI-driven program to obtain the pair distribution function from X-ray powder diffraction data, J. Appl. Crystallogr. 37 (4) (2004) 678, 678.

[24] T. Egami, S.J.L. Billinge, Underneath the Bragg Peaks Structural Analysis of Complex materials[M], Elsevier, 2003.

[25] A. Slipenyuk, J. Eckert, Correlation between enthalpy change and free volume reduction during structural relaxation of Zr55Cu30Al10Ni5 metallic glass, Scripta Mater. 50 (1) (2004) 39–44.

[26] S. Liu, L. Wang, J. Ge, Z. Wu, Y. Ke, Q. Li, B. Sun, T. Feng, Y. Wu, J.T. Wang, H. Hahn, Y. Ren, J.D. Almer, X.-l. Wang, S. Lan, Deformation-enhanced hierarchical multiscale structure heterogeneity in a Pd-Si bulk metallic glass, Acta Mater. 200 (2020) 42–55.

[27] D. Ma, A.D. Stoica, X.L. Wang, Power-law scaling and fractal nature of medium-range order in metallic glasses, Nat. Mater. 8 (1) (2008) 30–34.

[28] D. Turnbull, M.H. Cohen, On the free-volume model of the liquid-glass transition, J. Chem. Phys. 52 (6) (1970) 3038–3041.

[29] Y. Xu, J. Fang, H. Gleiter, H. Hahn, J. Li, Quantitative determination of free volume in $Pd_{40}Ni_{40}P_{20}$ bulk metallic glass, Scripta Mater. 62 (9) (2010) 674–677.

[30] H. Ding, P. Gong, W. Chen, Z. Peng, H. Bu, M. Zhang, X. Tang, J. Jin, L. Deng, G. Xie, X. Wang, K. Yao, J. Schroers, Achieving strength-ductility synergy in metallic glasses via electric current-enhanced structural fluctuations, Int. J. Plast. 169 (2023) 103711.

[31] S. Lan, Z. Wu, X. Wei, J. Zhou, Z. Lu, J. Neuefeind, X.-L. Wang, Structure origin of a transition of classic-to-avalanche nucleation in Zr-Cu-Al bulk metallic glasses, Acta Mater. 149 (2018) 108–118.

[32] D.A. Dimitrov, H. Röder, A.R. Bishop, Peak positions and shapes in neutron pair correlation functions from powders of highly anisotropic crystals, Phys. Rev. B 64 (1) (2001) 014303.

[33] D.B. Miracle, A structural model for metallic glasses, Microsc. Microanal. 10 (S02) (2004) 786–787.

[34] D. Ma, A.D. Stoica, L. Yang, X.-L. Wang, Z.P. Lu, J. Neuefeind, M.J. Kramer, J. W. Richardson, T. Proffen, Nearest-neighbor coordination and chemical ordering in multicomponent bulk metallic glasses, Appl. Phys. Lett. 90 (21) (2007) 211908.

[35] Z.Q. Ren, A.A. Churakova, X. Wang, S. Goel, S.N. Liu, Z.S. You, Y. Liu, S. Lan, D. V. Gunderov, J.T. Wang, R.Z. Valiev, Enhanced tensile strength and ductility of bulk metallic glasses $Zr_{52.5}Cu_{17.9}Al_{10}Ni_{14.6}Ti_5$ via high-pressure torsion, Mater. Sci. Eng., A 803 (2021) 140485.

[36] S. Lan, L. Zhu, Z. Wu, L. Gu, Q. Zhang, H. Kong, J. Liu, R. Song, S. Liu, G. Sha, Y. Wang, Q. Liu, W. Liu, P. Wang, C.-T. Liu, Y. Ren, X.-L. Wang, A medium-range structure motif linking amorphous and crystalline states, Nat. Mater. 20 (10) (2021) 1347–1352.

[37] J. Ding, E. Ma, Computational modeling sheds light on structural evolution in metallic glasses and supercooled liquids, npj Comput. Mater. 3 (1) (2017) 9.

[38] D. Ma, A.D. Stoica, X.L. Wang, Z.P. Lu, B. Clausen, D.W. Brown, Elastic moduli inheritance and the weakest link in bulk metallic glasses, Phys. Rev. Lett. 108 (8) (2012) 085501.

[39] J. Ding, E. Ma, M. Asta, R.O. Ritchie, Second-nearest-neighbor correlations from connection of atomic packing motifs in metallic glasses and liquids, Sci. Rep. 5 (1) (2015) 17429.

[40] C.A. Schuh, T.G. Nieh, A nanoindentation study of serrated flow in bulk metallic glasses, Acta Mater. 51 (2003) 87–99.

[41] T. Burgess, K.J. Laws, M. Ferry, Effect of loading rate on the serrated flow of a bulk metallic glass during nanoindentation, Acta Mater. 56 (17) (2008) 4829–4835.

[42] A.S. Argon, Plastic deformation in metallic glasses, Acta Metall. 27 (1) (1979) 47–58.

[43] M.C. Li, M.Q. Jiang, F. Jiang, L. He, J. Sun, Testing effects on hardness of a Zr-based metallic glass under nanoindentation, Scripta Mater. 138 (2017) 120–123.

[44] I.-C. Choi, Y. Zhao, Y.-J. Kim, B.-G. Yoo, J.-Y. Suh, U. Ramamurty, J.-i. Jang, Indentation size effect and shear transformation zone size in a bulk metallic glass in two different structural states, Acta Mater. 60 (19) (2012) 6862–6868.

[45] F. Dong, Y. Chu, M. He, Y. Zhang, W. Li, P.K. Liaw, B. Wang, L. Luo, Y. Su, R. O. Ritchie, X. Yuan, Manipulating internal flow units toward favorable plasticity in Zr-based bulk-metallic glasses by hydrogenation, J. Mater. Sci. Technol. 102 (2022) 36–45.

[46] W.L. Johnson, K. Samwer, A universal criterion for plastic yielding of metallic glasses with a $(T/T_g)^{2/3}$ temperature dependence, Phys. Rev. Lett. 95 (19) (2005) 195501.

[47] K. Mondal, T. Ohkubo, T. Mukai, K. Hono, Glass forming ability and mechanical properties of quinary Zr-based bulk metallic glasses, Mater. Trans. 48 (6) (2007) 1322–1326.

[48] J.D. Bernal, Geometry of the structure of monatomic liquids, Nature 185 (1960) 68–70.

[49] W.H. Jiang, F.X. Liu, Y.D. Wang, H.F. Zhang, H. Choo, P.K. Liaw, Comparison of mechanical behavior between bulk and ribbon Cu-based metallic glasses, Mater. Sci. Eng., A 430 (1–2) (2006) 350–354.

[50] L. Liu, K.C. Chan, Plastic deformation of Zr-based bulk metallic glasses under nanoindentation, Mater. Lett. 59 (24–25) (2005) 3090–3094.

[51] F. Spaepen, A microscopic mechanism for steady state inhomogeneous flow in metallic glasses, Acta Metall. 25 (1977) 407–415.

[52] F. Yang, Plastic flow in bulk metallic glasses: effect of strain rate, Appl. Phys. Lett. 91 (5) (2007).

[53] H. Zhang, Z. Wang, H.J. Yang, X.H. Shi, P.K. Liaw, J.W. Qiao, A flow model in bulk metallic glasses, Scripta Mater. 222 (2023) 115047.

[54] Y.S. Luo, Z. Wang, J. Eckert, J.W. Qiao, A universal criterion for the failure threshold in slowly sheared bulk metallic glasses, J. Appl. Phys. 129 (15) (2021) 155109.

[55] H. Zhang, Z. Wang, P.K. Liaw, J.W. Qiao, Y.C. Wu, A maximum temperature rise model of the shear band in bulk metallic glasses, J. Non-Cryst. Solids 626 (2024) 122806.

[56] M.T. Asadi Khanouki, R. Tavakoli, H. Aashuri, Effect of the strain rate on the intermediate temperature brittleness in Zr-based bulk metallic glasses, J. Non-Cryst. Solids 475 (2017) 172–178.

[57] J.H. Perepezko, S.D. Imhoff, M.W. Chen, J.Q. Wang, S. Gonzalez, Nucleation of shear bands in amorphous alloys, Proc. Natl. Acad. Sci. U.S.A. 111 (11) (2014) 3938–3942.

[58] J. Ketkaew, R. Yamada, H. Wang, D. Kuldinow, B.S. Schroers, W. Dmowski, T. Egami, J. Schroers, The effect of thermal cycling on the fracture toughness of metallic glasses, Acta Mater. 184 (2020) 100–108.

[59] D. Pan, A. Inoue, T. Sakurai, M.W. Chen, Experimental characterization of shear transformation zones for plastic flow of bulk metallic glasses, Proc. Natl. Acad. Sci. U.S.A. 105 (39) (2008) 14769–14772.

[60] J.W. Lv, F.L. Wang, D.W. Yin, S. Zhang, Z.Q. Cai, Z.L. Shi, M.Z. Ma, X.Y. Zhang, Effect of deep cryogenic cycling treatment on the microstructure and mechanical properties of Ti-based bulk metallic glass, J. Alloys Compd. 887 (2021) 161386.

[61] L. Hu, C. Zhang, Y. Yue, Structural evolution during the sub-Tg relaxation of hyperquenched metallic glasses, Appl. Phys. Lett. 96 (22) (2010) 221908.

[62] F. Dong, M. He, Y. Zhang, B. Wang, L. Luo, Y. Su, H. Yang, X. Yuan, Investigation of shear transformation zone and ductility of Zr-based bulk metallic glass after plasma-assisted hydrogenation, Mater. Sci. Eng., A 759 (2019) 105–111.